

Detection by voxel-wise statistical analysis of significant changes in regional cerebral glucose uptake in an APP/PS1 transgenic mouse model of Alzheimer's disease

Albertine Dubois^{a,b,*}, Anne-Sophie Hérard^a, Benoît Delatour^c, Philippe Hantraye^a, Gilles Bonvento^a, Marc Dhenain^a, Thierry Delzescaux^a

^a CEA-DSV-I2BM-MIRCen-LMN, Orsay, France

^b CEA-DSV-I2BM-Neurospin-LRMN, Gif-sur-Yvette, France

^c CNRS UMR 8620, Orsay, France

ARTICLE INFO

Article history:

Received 16 November 2009

Revised 17 February 2010

Accepted 25 February 2010

Available online xxxx

Keywords:

3D reconstruction

Voxel-wise statistical analysis

Transgenic mouse brain

Alzheimer's disease

Cerebral glucose uptake

Autoradiography

ABSTRACT

Biomarkers and technologies similar to those used in humans are essential for the follow-up of Alzheimer's disease (AD) animal models, particularly for the clarification of mechanisms and the screening and validation of new candidate treatments. In humans, changes in brain metabolism can be detected by 1-deoxy-2-[¹⁸F] fluoro-D-glucose PET (FDG-PET) and assessed in a user-independent manner with dedicated software, such as Statistical Parametric Mapping (SPM). FDG-PET can be carried out in small animals, but its resolution is low as compared to the size of rodent brain structures. In mouse models of AD, changes in cerebral glucose utilization are usually detected by [¹⁴C]-2-deoxyglucose (2DG) autoradiography, but this requires prior manual outlining of regions of interest (ROI) on selected sections. Here, we evaluate the feasibility of applying the SPM method to 3D autoradiographic data sets mapping brain metabolic activity in a transgenic mouse model of AD. We report the preliminary results obtained with 4 APP/PS1 (64 ± 1 weeks) and 3 PS1 (65 ± 2 weeks) mice. We also describe new procedures for the acquisition and use of "blockface" photographs and provide the first demonstration of their value for the 3D reconstruction and spatial normalization of *post mortem* mouse brain volumes. Despite this limited sample size, our results appear to be meaningful, consistent, and more comprehensive than findings from previously published studies based on conventional ROI-based methods. The establishment of statistical significance at the voxel level, rather than with a user-defined ROI, makes it possible to detect more reliably subtle differences in geometrically complex regions, such as the hippocampus. Our approach is generic and could be easily applied to other biomarkers and extended to other species and applications.

© 2010 Published by Elsevier Inc.

Introduction

Alzheimer's disease (AD) is a neurodegenerative process leading to progressive and irreversible impairments of cognition and behavior. It is associated with a severe neuronal loss, and the accumulation of amyloid- β (A β) plaques and neurofibrillary tangles (NFT) (Goedert and Spillantini, 2006).

Definitive diagnosis of AD still requires the *post mortem* examination of brain tissue, to obtain evidence that these specific neuropathological lesions are present. Over the last 30 years, considerable progress has been made in the development of biomarkers to bridge the gap between the "gold standard" of *post mortem* neuropathological confirmation and the clinical diagnosis of AD on the basis of cognitive deficits and the exclusion of other dementia disorders. Among other techniques, functional neuroimaging with positron

emission tomography (PET) is being investigated as a possible source of biomarkers for AD. In particular, 1-deoxy-2-[¹⁸F] fluoro-D-glucose (FDG)-PET detects changes in cerebral metabolism during both the prodromal and clinical phases of AD. It is highly sensitive and can thus identify target structures at high risk of disruption by AD (Reiman et al., 1996; Minoshima et al., 1997). Recently developed PET tracers, such as Pittsburgh Compound B (PIB) and 2-(1-6-[(2-18F-fluoroethyl) (methyl)amino]2-naphthylethylidene)-malononitrile (FDDNP) have been used to visualize A β plaques and NFT in AD patients (Shoghi-Jadid et al., 2002; Klunk et al., 2004; Small et al., 2006). FDDNP binds to both amyloid plaques and tangles, whereas PIB selectively labels amyloid plaques.

Several potential treatments for AD are currently being developed and are tested in transgenic animal models – mostly mice – overexpressing a mutated form of the human A β precursor protein (APP) gene associated with familial forms of AD. Both single (PDAPP, (Games et al., 1995); Tg2576, (Hsiao et al., 1996) and double (APP \times mutated PS1, PSAPP) transgenic mice develop plaques in the brain. However, co-expression with the gene encoding human

* Corresponding author. CEA-DSV-I2BM-SHFJ Inserm U803, 4 place du Général Leclerc, 91401 Orsay Cedex, France. Fax: +33 1 69 86 77 45.

E-mail address: albertine.dubois@cea.fr (A. Dubois).

mutated presenilin 1 significantly decreases the age at which the first plaques are detected (Duff et al., 1996; Holcomb et al., 1998). The pathological features observed in these APP and PSAPP transgenic mice include diffuse amyloid deposits and dense core (fibrillar) plaques mimicking the senile plaques of human AD patients. These transgenic mice provide a means to detect and track biomarker changes similar to those observed in humans. They are therefore of potential interest in the understanding of the disease mechanisms, such as biological aspects of the changes in cerebral glucose utilization, and the preclinical screening of new disease-slowing treatments.

(FDG)-PET can be performed in small animals, but its spatial resolution (~0.5 to 3 mm) is low as compared to the size of rodent brain structures, making it impossible to avoid the inclusion of tissues with different rates of metabolism within a single voxel or region of interest (ROI). In mouse models of AD, changes in cerebral glucose utilization are therefore usually detected by high-resolution autoradiography (~100–200 μm), which remains the reference technique for functional neuroimaging in small-animal research. Quantitative autoradiographic studies are classically analyzed through manual segmentation of ROIs on a limited number of 2D sections (Dodart et al., 1999; Reiman et al., 2000; Niwa et al., 2002; Sadowski et al., 2004; Valla et al., 2006). These techniques, however, may be subject to observer bias and inaccurate manual delineation, particularly when the ROI is defined directly on autoradiographic modality images. Moreover, ROI-based analyses are intrinsically hypothesis-driven, and significant effects in areas away from the pre-defined ROIs may be overlooked.

The inherent limitations of ROI-based analysis have been tackled by the use of methods combining data from different subjects into a common spatial referential. This spatial normalization of data from individual subjects to a standardized brain volume makes it possible to use voxel-wise statistical analysis for group comparisons. The recent application of these methods to 3D-reconstructed autoradiographic images led to the identification of significant functional differences in various brain regions, between two groups of rats in specific experimental conditions (treadmill walking, (Nguyen et al., 2004); cortical deafness model, (Lee et al., 2005); conditioned fear, (Holschneider et al., 2006); and visual stimulus, (Dubois et al., 2008b)). In the current study, we evaluated the feasibility and the reliability of applying spatial normalization and voxel-wise statistical analysis to 3D autoradiographic data sets first time mapping brain metabolic activity in a mouse model of AD (smallest brain structures and species investigated so far). We report the preliminary results obtained in such a pathological context with a limited sample size ($n=7$). We also describe new procedures for the acquisition and use of photographs of the brain face taken during sectioning, generally referred to as “blockface photographs”, and provide the first demonstration of their value for the 3D reconstruction and spatial normalization of *post mortem* mouse brain volumes. Despite being limited by the relatively small sample size, we discuss the reliability of our preliminary findings and the likely contribution of voxel-wise analysis to increasing knowledge about neurodegenerative diseases and to the efficient development and exhaustive validation of new therapeutic approaches.

Materials and methods

Animals

Experiments were conducted on adult APP/PS1 transgenic mice. This transgenic line is based on the overexpression of both human amyloid precursor protein (APP driven by the Thy-1 promoter and harboring three familial mutations, the Swedish K670M/N671L and London V717I mutations) and mutant presenilin 1 (PS1 with the M146L mutation). The mutated presenilin 1 gene accelerates amyloid

deposition (Blanchard et al., 2003). In these transgenic mice, amyloid deposition begins at the age of 2.5 months (Wirhns et al., 2001). Heterozygous APP/PS1 mice were obtained by crossing heterozygous transgenic APP_(+/-) mice with homozygous transgenic PS1_(+/-) mice. The APP_(-/-)/PS1_(+/-) mouse littermates (PS1) resulting from crossings were used as controls as they display no amyloid plaques and can therefore allow to specifically evaluate the effects of the APP transgene on amyloid deposition in the brain (Delatour et al., 2006; El Tannir El Tayara et al., 2006; Dhenain et al., 2009). All the procedures were designed to minimize animal suffering and were carried out in accordance with the recommendations of the EEC (86/609/EEC) and the French National Committee (87/848) for the use of laboratory animals.

Measurement of [¹⁴C]-2-deoxyglucose (2-DG) uptake

We measured 2-DG uptake in 4 APP/PS1 (64 ± 1 weeks) and 3 PS1 (65 ± 2 weeks) mice. Experiments were performed on conscious, lightly restrained animals. Animals were fasted but had free access to water for 12 h before the experiment. On the day of the experiment, mice were anesthetized with isoflurane and a catheter was inserted intraperitoneally. Body temperature was monitored rectally and maintained at 37 °C with a thermostatically controlled heating pad. Mice were allowed to recover from anesthesia for 1 h and were then injected with 2-DG (16.5 μCi/100 g body weight). Uptake occurred over a period of 45 min and the animals were then euthanized by injection of a lethal dose of sodium pentobarbital. The entire brain was removed and split into its left and right hemispheres. For each animal, we evaluated cerebral glucose uptake in the right hemisphere by quantitative autoradiography, whereas the left hemisphere was processed for amyloid deposit detection by standard Congo red staining.

Congo red staining

The left hemispheres were fixed in 10% buffered formalin and stored in this fixative, at 4 °C, until processing for histology. They were cut into 40 μm-thick coronal sections on a freezing microtome after cryoprotection in 20% glycerin and 2% dimethyl sulfoxide in 0.1 M phosphate buffer. Amyloid deposits were labeled by standard Congo red staining (incubation for 30 min in an 80% ethanol solution saturated with Congo red and sodium chloride). Each Congo red-stained section was digitized, using a high-resolution flatbed scanner with 4000 dpi in-plane resolution (pixel size 6.35 × 6.35 μm²).

Data acquisition and 3D reconstruction of blockface, autoradiographic and histological *post mortem* volumes

The right hemispheres, destined for autoradiography, were snap-frozen in isopentane at -40 °C. They were then embedded in a custom-made mixture of M1 embedding matrix (Shandon, Pittsburg, PA, USA) and Fast Green (Sigma-Aldrich, Lyon, France) and cut into 20 μm-thick coronal sections on a cryostat. Every fourth section was mounted on Superfrost glass slides, rapidly heat-dried and placed against autoradiographic film for one week, together with radioactive [¹⁴C] standards. The same sections were then processed for Nissl staining. The olfactory bulb and the cerebellum were excluded from the sectioning process.

Blockface volume

Images from the surface of the frozen hemisphere were recorded with a digital camera (Canon Powershot G5 Pro) before the cutting of each fourth section. These photographs were taken at the end of the cryostat wheel crank course, ensuring that the brain was in the same position for all sections (X and Y axes) and at the same distance from the camera (Z axis). An optic fiber-ring light was fixed onto the

203 objective of the camera. This provided uniform, reproducible
 204 illumination of the sample. A computer was used to control the
 205 camera, making it possible to take images remotely, and the images
 206 were stored directly on this computer. For each right hemisphere, we
 207 obtained a series of about 120 blockface photographs with an in-plane
 208 resolution of $27 \times 27 \mu\text{m}^2$ (Fig. 1A). The calibration factor between the
 209 number of pixels in the images and the corresponding distance in
 210 millimeters was determined by obtaining an image of a piece of graph
 211 paper in the focal plane before sectioning. To reduce the field of view,
 212 the photographs were first cropped manually by interactively
 213 selecting the four points defining the coordinates of the right, left,
 214 top and bottom borders (Fig. 1B). They were then automatically
 215 segmented to separate the brain tissue from the embedding medium
 216 and to set the background to zero (Fig. 1C). Series of segmented
 217 photographs were stacked in the Z direction, to create a 3D consistent
 218 blockface volume (Fig. 1D). No registration was required due to the
 219 natural spatial consistency of the images.

Autoradiographic and histological volumes

220 The autoradiographs, the corresponding Nissl-stained sections and
 221 the ^{14}C standards were digitized as 8-bit gray-scale images, using a
 222 flatbed scanner with 1200 dpi in-plane resolution (pixel size
 223 $21 \times 21 \mu\text{m}^2$). As previously described (Dubois et al., 2007), the
 224 sections were extracted from the scans, individualized, stacked in the
 225 Z direction and rigidly registered so as to obtain spatially consistent
 226 3D volumes. Corresponding computerized procedures are now
 227 included in our in-house image processing software, BrainVISA,
 228 which can be freely downloaded from the Internet (<http://brainvisa.info/downloadpage.html>). They are collected into an add-on module
 229 package, called Brain Reconstruction and Analysis Toolbox (BrainRAT)
 230 and available for version 3.1.4 and higher (personal communication:
 231 Dubois et al., 2008a).
 232

233 First applications of voxel-wise statistical analysis to *post mortem*
 234 data solely required the alignment of 2D autoradiographic sections
 235 into a 3D volume (Nguyen et al., 2004; Lee et al., 2005; Holschneider
 236

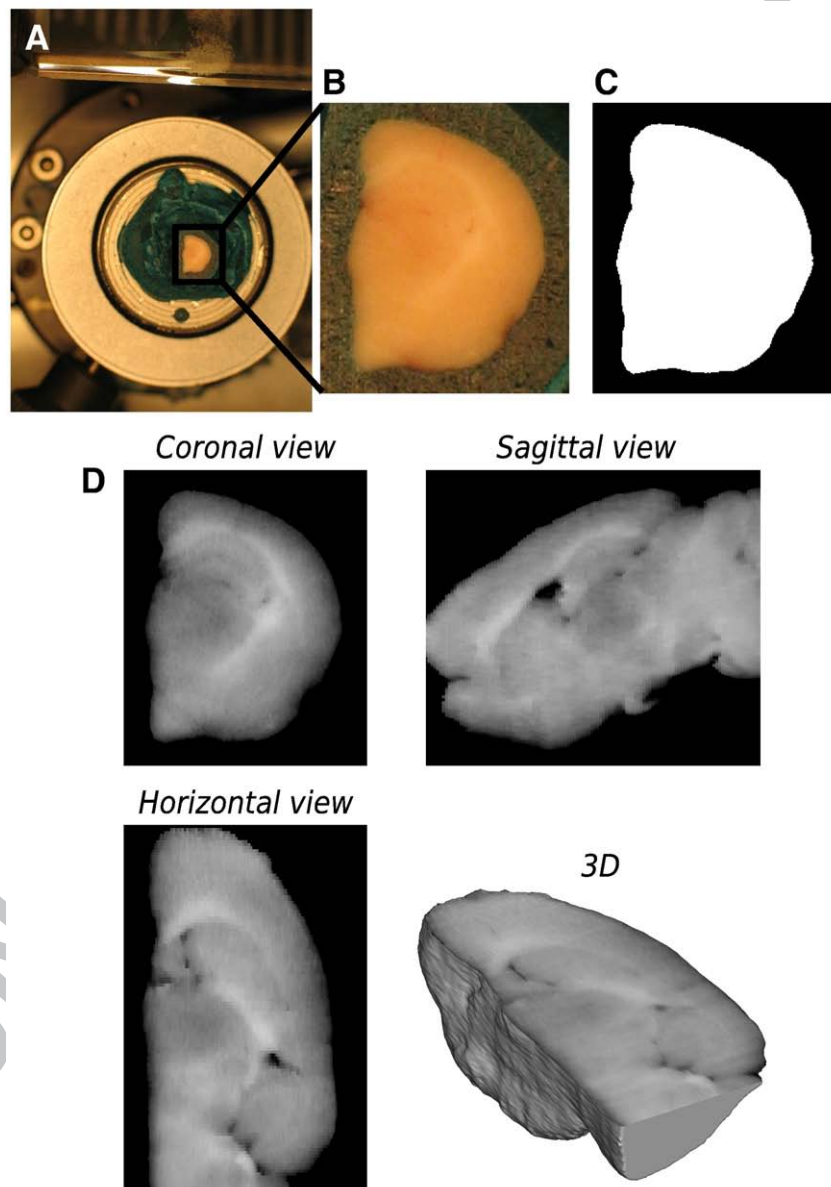


Fig. 1. (A) Blockface photograph of one mouse hemisphere recorded with a digital camera. (B) The same blockface photograph, obtained after reducing the field of view. (C) Corresponding binary image obtained after separation of the brain tissue from the embedding medium, by setting the background to zero. (D) Blockface volume, achieved by stacking the series of segmented photographs (green component obtained after RGB separation) in the Z direction. This volume is represented in three orthogonal views and as a 3D volume-rendered image. (For interpretation of the references to color in this figure legend, the reader is referred to the web version of this article.)

et al., 2006; Holschneider and Maarek, 2008). In our previous work (Dubois et al., 2008b), we better used a co-registration strategy of autoradiographic with corresponding histological sections, benefiting from greater anatomical detail provided by Nissl staining as compared to autoradiography. In the current study, we dealt with three different imaging modalities: autoradiography, histology and blockface photography. We therefore proposed an original strategy for 3D reconstruction of *post mortem* volume images (Fig. 2), combining 1) co-registration of each histological section with its corresponding photograph from the blockface volume (HistoScheme 1) and 2) co-registration of each autoradiographic section with its corresponding registered histological section (AutoradScheme 1).

To validate this approach, we first compared the histological volume reconstructed with HistoScheme 1 to that resulting from the registration of each histological section with a reference one in the stack, using a propagation-based approach as described by (Dubois et al., 2007) (HistoScheme 2). The consistency of each 3D-reconstructed histological volume was assessed by visual inspection of internal structures viewed in different orthogonal incidences and by visual inspection of the 3D surface renderings of the corresponding volumes. The blockface volume was used as a reference for the comparison of the two methods. We also compared the anatomo-functional superimposition obtained with AutoradScheme 1 to that derived from the co-registration of each 2D autoradiographic section with its corresponding blockface photograph from the blockface volume (AutoradScheme 2). The accuracy of anatomo-functional superimpositions was assessed by superimposing the histological volumes from the 7 hemispheres onto their corresponding autoradiographic volumes.

Lastly, the gray-scale level intensities were calibrated, using the co-exposed [^{14}C] standard scale, and converted to activity values (nCi/g of tissue).

Creation of a study-specific template and spatial normalization

Individual 3D-reconstructed autoradiographic volumes for each right hemisphere were spatially normalized into a standardized coordinate space defined by a study-specific template of the mouse right hemisphere. Creation of such a template has been described in previous works (Nguyen et al., 2004; Lee et al., 2005; Dubois et al., 2008b). Spatial normalization was achieved by applying a 12-parameter affine transformation and then estimating non-linear deformations with a linear combination of 3D discrete cosine transform basis functions (Ashburner and Friston, 1999). Spatially

normalized hemispheres from all seven mice were then individually smoothed with a Gaussian kernel (FWHM=3 times the voxel dimensions) for further processing. Given the voxel dimensions, $21 \times 21 \times 80 \mu\text{m}^3$, the final spatial resolution of the smoothed images was $63 \times 63 \times 240 \mu\text{m}^3$, which was compatible with estimate of misregistration error and anatomic variability (Nguyen et al., 2004). The template of the mouse right hemisphere was created and spatial normalization was carried out with the SPM5 software package (<http://www.fil.ion.ucl.ac.uk/spm/>).

In a previous study (Dubois et al., 2008b), we compared two spatial normalization techniques based on a histological or autoradiographic template. We found that histological template-based method did not provide accurate spatial normalizations and failed to reach the high level of spatial specificity obtained with autoradiographic template-based method. The autoradiographic template was therefore more appropriate for spatial normalization than the histological template. In the present study, we also compared the autoradiographic template-based method with a blockface photographic template-based method. With the blockface template, deformation parameters were calculated entirely from a photographic template and then applied to the corresponding autoradiographic volume images. The accuracy of the spatial normalization techniques based on photographic and autoradiographic templates was assessed by calculating voxel-by-voxel mean and standard deviation images of spatially normalized autoradiographic volumes from PS1 and APP/PS1 hemispheres, separately (Ashburner and Friston, 1999).

Statistical design and analysis in SPM

Overall differences in the absolute amount of radiotracer delivered to the brain were beforehand adjusted in each animal by scaling the voxel intensities so that the mean intensity for all seven hemispheres studied was the same. Regional differences in cerebral glucose uptake between APP/PS1 and PS1 transgenic mice were then assessed with SPM5 software. We subtracted the background and excluded the lateral ventricle from the analysis and performed the SPM5 two-sample *t*-test. Two contrasts were evaluated separately, making it possible to produce two statistical parametric maps: maps showing voxels of lower intensity in APP/PS1 than in PS1 mice (lower levels of glucose uptake in APP/PS1 than in PS1 mice) and maps displaying voxels of higher intensity in APP/PS1 than in PS1 animals (higher levels of glucose uptake in APP/PS1 than in PS1 mice). As in previous studies, we considered $P < 0.01$ (uncorrected for multiple comparisons) to indicate statistical significance for individual voxels within

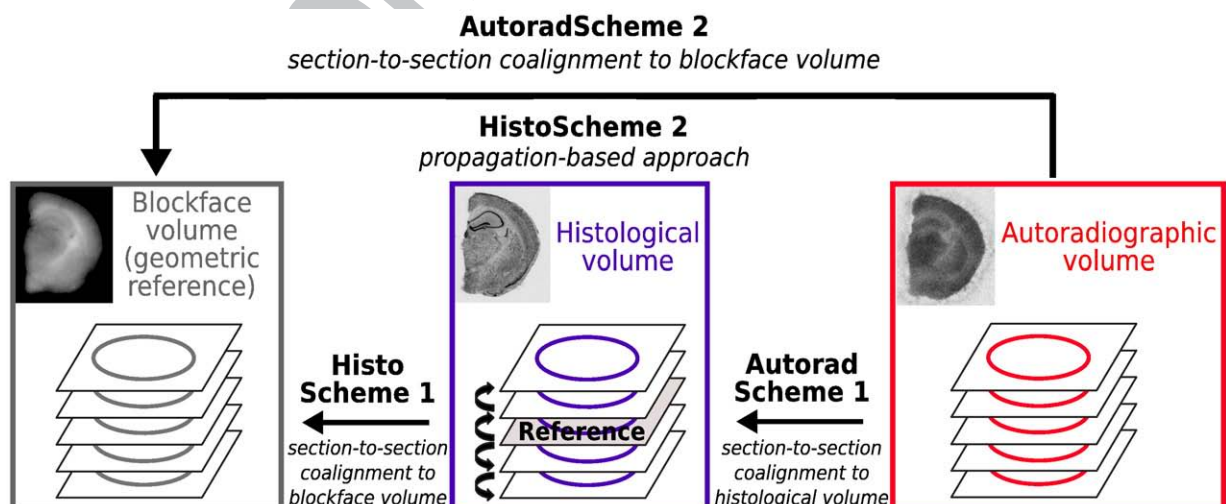


Fig. 2. Summary chart for the two different methods for 3D reconstruction of the histological (HistoSchemes 1 and 2) and autoradiographic (AutoradSchemes 1 and 2) volumes.

321 clusters of contiguous voxels, and we used a minimum cluster size of
 322 1500 contiguous voxels, amounting to $\sim 0.05 \text{ mm}^3$, with a resolution
 323 of $21 \times 21 \times 80 \mu\text{m}^3$. We then evaluated the location of significant
 324 voxels within the whole hemisphere and the significance of clusters of
 325 contiguous voxels exceeding the minimum cluster size. The Marsbar
 326 toolbox included in SPM5 (Brett et al., 2003) was used to calculate the
 327 mean intensity (i.e., activity) for each cluster. Brain regions were
 328 identified with an anatomical atlas of the mouse brain (Paxinos and
 329 Franklin, 2001).

330 The impact of the two spatial normalization techniques on the
 331 voxel-wise statistical analysis was also evaluated. For each contrast,
 332 the set of results obtained with the photographic template-based
 333 normalization method was compared with those obtained with the
 334 autoradiographic template.

335 Results

336 Cerebral A β deposition

337 Congo red staining revealed numerous A β deposits in the left
 338 hemispheres of APP/PS1 mice (Fig. 3A). Amyloid deposits were mostly
 339 observed in iso- and archicortical (hippocampus) brain areas and in
 340 certain subcortical regions (e.g., thalamus, septal nuclei, amygdala,

341 accumbens nucleus), as previously shown (Blanchard et al., 2003;
 342 Delatour et al., 2006). Within the hippocampus, plaques were limited
 343 to the outer and inner part of the molecular layer of the dentate gyrus
 344 and the stratum lacunosum moleculare of CA1. PS1 animals had no
 345 amyloid deposits, as expected (Fig. 3B).

Data acquisition and 3D reconstruction of blockface, autoradiographic and histological post mortem volumes

348 For each series of blockface photographs, the automatic segmen-
 349 tation successfully separated the brain tissue from the embedding
 350 medium, making it possible to remove background from images. For
 351 each mouse, a spatially consistent 3D blockface volume was obtained
 352 by directly stacking the series of photographs. No registration was
 353 required due to reproducible positioning of the tissue in the cutting
 354 plane before the cutting of each section.

355 The evaluation of the consistency of each 3D-reconstructed
 356 histological volume demonstrated that, globally, HistoScheme 1 was
 357 more reliable than HistoScheme 2. Indeed, the discontinuities
 358 between consecutive histological sections, due to possible registration
 359 errors, were greater with HistoScheme 2 than with HistoScheme 1
 360 (black arrows in Figs. 4A and C). In addition, the overall shape and
 361 geometry of the histological volume reconstructed with HistoScheme
 362 1 more closely resembled those of the blockface volume than did
 363 those obtained with HistoScheme 2 (Figs. 4B and D). As the blockface
 364 volume was regarded as a consistent 3D geometric reference, closely
 365 resembling the original geometry *in vivo*, HistoScheme 1 was
 366 therefore considered to ensure greater intra-volume consistency in
 367 the 3D-reconstructed histological volume than HistoScheme 2.
 368 Nevertheless, the histological volume reconstructed with HistoScheme
 369 2 presented a slightly higher definition and morphological accuracy
 370 of inner structures, including the striatum (CPu), the corpus
 371 callosum (cc) and the hippocampus (Hp).

372 The evaluation of the quality of anatomo-functional superimposi-
 373 tions showed AutoradScheme 1 to be more reliable than AutoradScheme
 374 2. Indeed, with AutoradScheme 1, the external contours (Ext) and the
 375 outer edges of the cortex (OutCx), subcortical structures (e.g., corpus
 376 callosum (cc)) and A β plaque-like deposits (A β) in the histological
 377 volume (Figs. 5A, B and C) were correctly superimposed onto the
 378 same areas in the corresponding autoradiographic volume (Figs. 5D
 379 and F). By contrast, AutoradScheme 2 led to misregistrations and
 380 incorrect superimpositions in some cases, resulting in lower
 381 inter-volume consistency (Figs. 5E and G).

382 Thus, the best global strategy for the 3D reconstruction of both
 383 histological and autoradiographic volumes from all seven mice was
 384 our proposed approach *i.e.* combining HistoScheme 1 and Auto-
 385 radScheme 1.

Spatial normalization: comparison of photographic and functional templates

388 The two different spatial normalization techniques based on
 389 photographic and autoradiographic templates were compared (Fig. 6A)
 390 and shown to provide similar results for both PS1 and APP/PS1
 391 hemispheres (Figs. 6B and C, respectively). Indeed, the mean
 392 images obtained with both template-based normalization methods
 393 displayed similar levels of contrast for the various structures in the
 394 brain of PS1 or APP/PS1 mice. Sharpness and the consistency of
 395 contours for the various structures were equivalent in all cases,
 396 regardless of the method used. The standard deviation images from
 397 PS1 or APP/PS1 mice showed similar values, demonstrating that the
 398 intensity differences between normalized hemispheres were similar.
 399 However, differences at the outer edges of the cortex appeared to be
 400 less marked with the autoradiographic template than with the
 401 photographic method. Another comparison involved superimposition
 402 of the edge contours calculated from the normalized reference

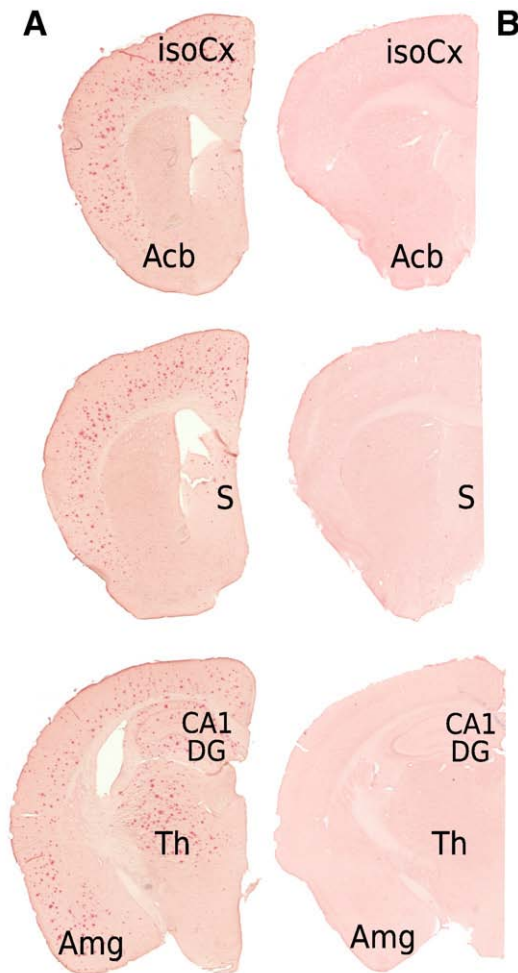


Fig. 3. Coronal antero-posterior Congo red-stained sections from left hemisphere of one APP/PS1 (A) and one PS1 (B) mice. Note the high density of A β deposits in iso- and archicortical brain areas (isoCx), accumbens nucleus (Acb), septal nuclei (S), hippocampus, thalamus (Th) and amygdala (Amg). In the hippocampus, plaques are limited to the outer and inner parts of the molecular layer of the dentate gyrus (DG) and stratum lacunosum moleculare of CA1 (CA1). PS1 animals did not show any amyloid deposits.

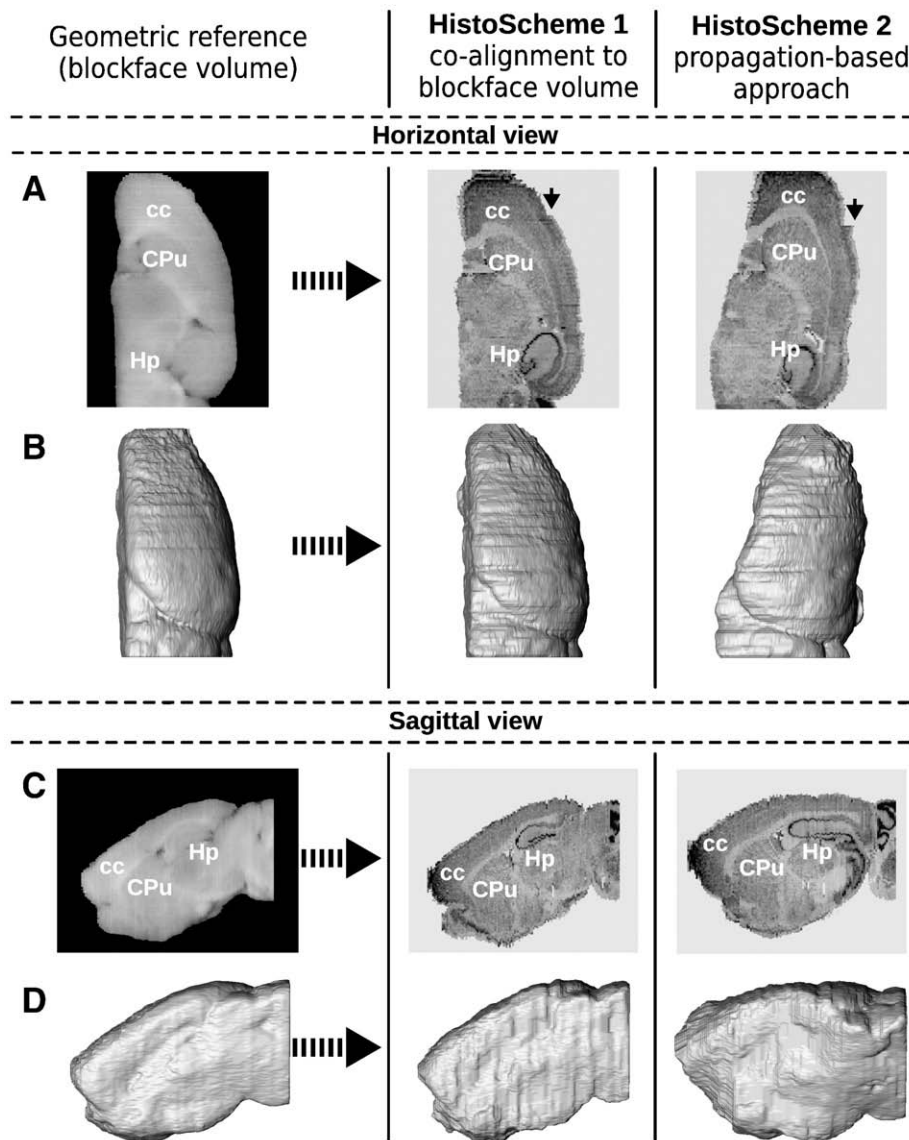


Fig. 4. Evaluation of the two methods for 3D reconstruction of the histological volume. Histological volume and corresponding 3D surface rendering in horizontal (A and B) and sagittal (C and D) views obtained from one mouse hemisphere by co-registering each histological section with its corresponding photograph from the blockface volume (HistoScheme 1; middle panel) or by registering each histological section with a reference section in the stack, using a propagative approach, as described by citetDubois07a (HistoScheme 2; right panel). The blockface volume from the same animal and its corresponding 3D surface rendering are displayed in the same view and used as a reference for the comparison of the two methods (left panel). cc: corpus callosum, Hp: hippocampus and CPu: striatum.

hemisphere used to generate both the photographic and autoradiographic templates onto the spatially normalized autoradiographic data from individual mice (Fig. 6C). The photographic template-based normalization method led to slight misregistrations of the outer edges of the cortex. However, with both template-based normalization methods, the edges defining the subcortical structures, such as the striatum, thalamus and inner edges of the cortex in the template were correctly superimposed onto the same structures in each of the 7 normalized hemispheres.

As both template-based methods appeared to be suitable for the spatial normalization of 3D-reconstructed autoradiographic volumes, we additionally compared the statistical outcome of each method in subsequent voxel-wise analysis, to determine if one or the other of these approaches performed better.

Statistical analysis

Brain regions with cluster-level significant differences in glucose uptake between APP/PS1 and PS1 transgenic mice are displayed in

Fig. 7. In this figure, the color-coded statistical maps of t values represent the results of the voxel-wise statistical group comparison between the 4 APP/PS1 and the 3 PS1 hemispheres, using an uncorrected P value of $P < 0.01$. These maps were overlaid on several coronal stained histological sections from a spatially normalized hemisphere, to facilitate the identification of brain regions. Clusters of significant differences in glucose uptake between animals are also represented as 3D volume-rendered images.

Differences between statistical t maps for voxel-wise analysis with photographic and autoradiographic template-based normalization methods are summarized in Tables 1 and 2. Clusters exceeding the threshold and displaying a significant difference in glucose uptake between animals were obtained within the same anatomical brain structures with both templates. They also had similar P values and covered a similar area. Limited differences in the detection sensitivity and morphology terms were found between the two normalization methods. Hence, neither the assessment of accuracy nor the statistical outcome of the two different spatial normalization techniques in subsequent voxel-wise analysis was sufficiently discriminating to

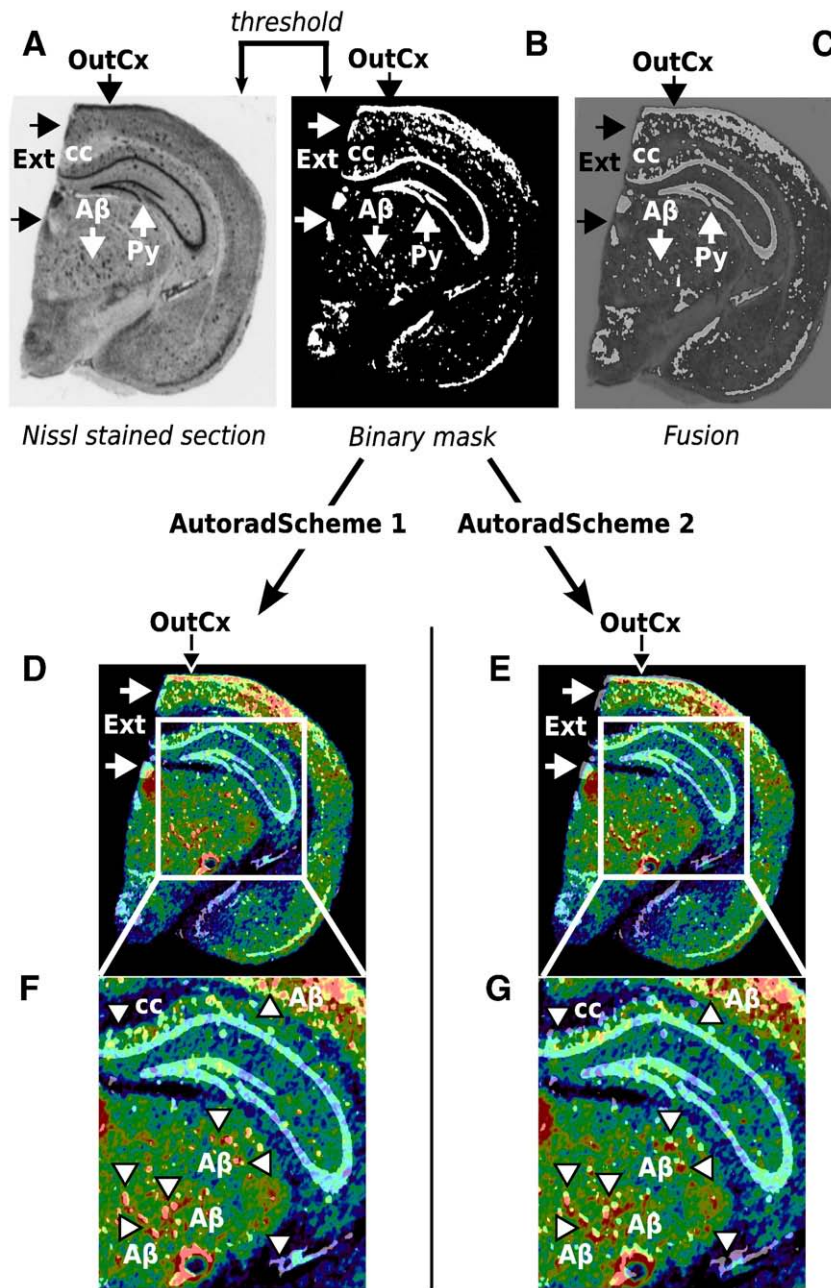


Fig. 5. Evaluation of the two methods for 3D reconstruction of the autoradiographic volume. (A) Nissl-stained section extracted from the histological volume of one APP/PS1 mouse hemisphere. (B) Binary image of the same section, result of a threshold operation. (C) Superimposition of (A) and (B). External contours (Ext), outer edges of the cortex (OutCx), pyramidal cell layers of the hippocampus (Py) and A- β plaque-like deposits (A β) are shown in white. (D) and (E) Superimposition of (B) onto the corresponding autoradiographic section. Images on the left were derived using AutoradScheme 1; those on the right were derived using AutoradScheme 2. Note the misregistrations of Ext and OutCx with AutoradScheme 2 (black and white arrows). (F) and (G) Magnification of the hippocampal and thalamic regions, showing incorrect superimpositions with AutoradScheme 2 concerning the location of the corpus callosum (cc; dark blue area) and A β deposits (A β ; hyperintense red spots, arrowheads) as compared to superimposition with AutoradScheme 1. (For interpretation of the references to color in this figure legend, the reader is referred to the web version of this article.)

439 identify one method as being better than the other. Given these
440 findings, we chose to analyze further only the results obtained with
441 the photographic template-based normalization method.

442 Glucose uptake levels were lower in APP/PS1 than in PS1 mice
443 mostly within the cortical (cingulate, retrosplenial and somatosensory),
444 striatal and thalamic regions, as well as hippocampal regions
445 (lacunosum moleculare and radial layers of the CA1 and CA3 regions).
446 Regions of higher levels of glucose uptake were also detected in other
447 cortex areas (piriform and perirhinal) in these mice, and in the
448 amygdaloid, dorsal endopiriform and accumbens nuclei, the dentate
449 gyrus and the dorsal part of the hippocampus (oriens and pyramidal
450 cell layers of the CA1 and CA3 regions).

The differences in activity (percentage), obtained with the
Marsbar toolbox from the statistical analysis are presented in
Table 3. This table illustrates the low inter-individual variability in
activity values for animals of a given genotype. Indeed, in APP/PS1 and
PS1 mice, each region of higher or lower glucose uptake presented a
coefficient of variation of less than 5%. Much greater inter-individual
variability in activity values between genotypes was observed. Indeed,
the percentage difference between the mean activity values in APP/
PS1 and PS1 mice, measured for all clusters of significant difference in
glucose uptake detected by the statistical analysis, was about 20%. The
activity in the hippocampus (the lacunosum moleculare and radial
layers) of APP/PS1 mice was 24.6% lower than in PS1 mice. Activity

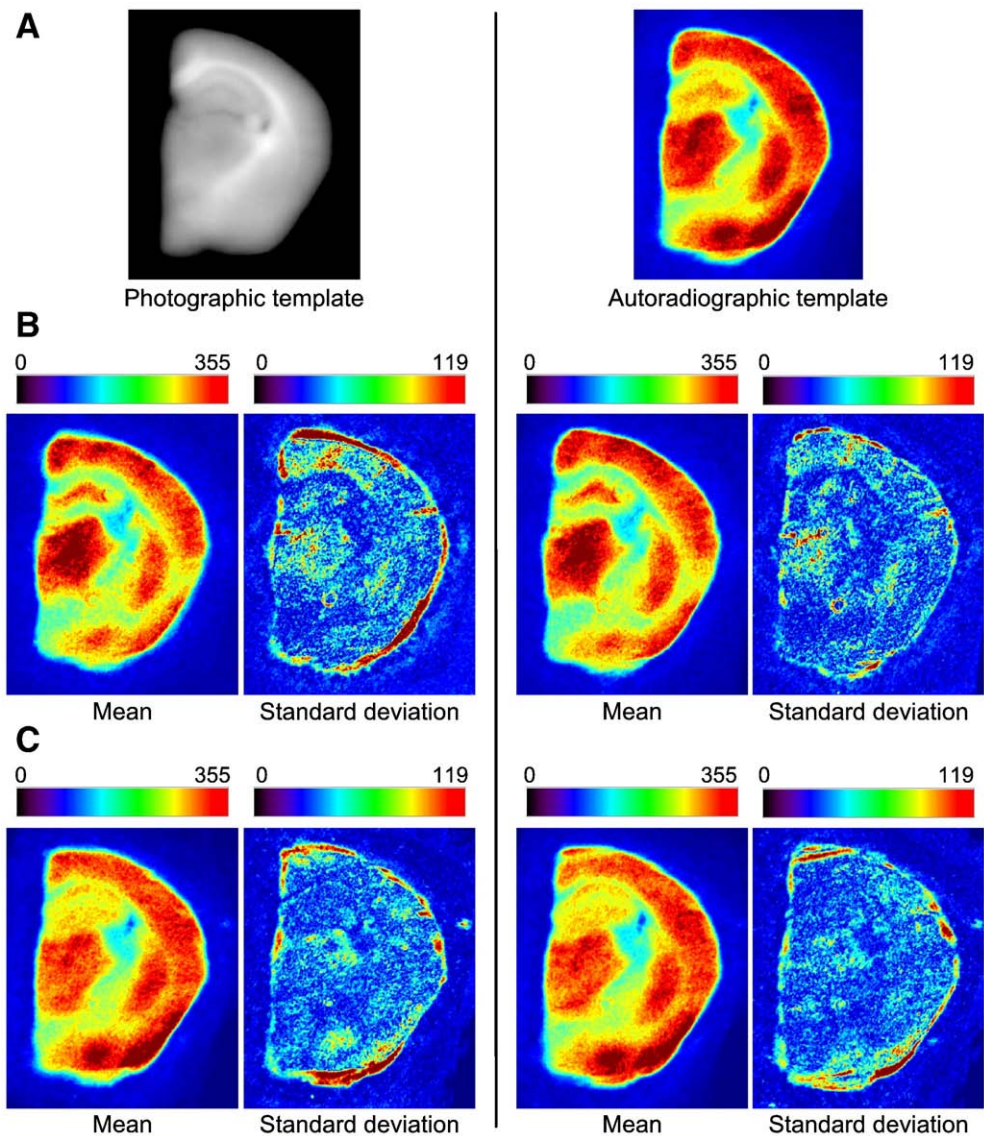


Fig. 6. Evaluation of spatial normalization with study-specific templates. (A) Photographic and autoradiographic templates. (B) Mean and standard deviation of spatially normalized 3D autoradiographic volume images from PS1 hemispheres. (C) Mean and standard deviation of spatially normalized 3D autoradiographic volume images from APP/PS1 hemispheres. Images on the left were derived using the photographic template; those on the right were derived using the autoradiographic template. (C) Superimposition of the contours of the normalized reference hemisphere used to generate both photographic and autoradiographic templates onto the spatially normalized hemisphere of another mouse after spatial normalization with the photographic and autoradiographic templates, respectively.

463 levels were 23.3% lower in the somatosensory cortex, 35.6% lower in
 464 the cingulate cortex, 26.1% lower in the retrosplenial cortex, 22.4%
 465 lower in the striatum and 28.8% lower in the thalamus. As mentioned
 466 above, the voxel-wise analysis revealed the existence of regions with
 467 significantly higher levels of glucose uptake. This uptake activity was
 468 25.8% higher in the oriens and pyramidal cell layers of the
 469 hippocampus, 25.2% higher in the dentate gyrus, 22.9% higher in the
 470 amygdala, 33.7% higher and 20.4% higher in the dorsal endopiriform
 471 and accumbens nuclei, respectively, 21.5% higher in the piriform
 472 cortex and 19.3% higher in the perirhinal cortex.

473 Discussion

474 In this study, we evaluated the feasibility to apply our analysis
 475 method, combining computerized procedures for the acquisition
 476 and 3D reconstruction of autoradiographic volume images, spatial
 477 normalization, and voxel-wise statistical analysis (Dubois et al.,
 478 2008b) to autoradiographic data mapping brain metabolic activity
 479 in a mouse model of AD. Because mice are widely used models for

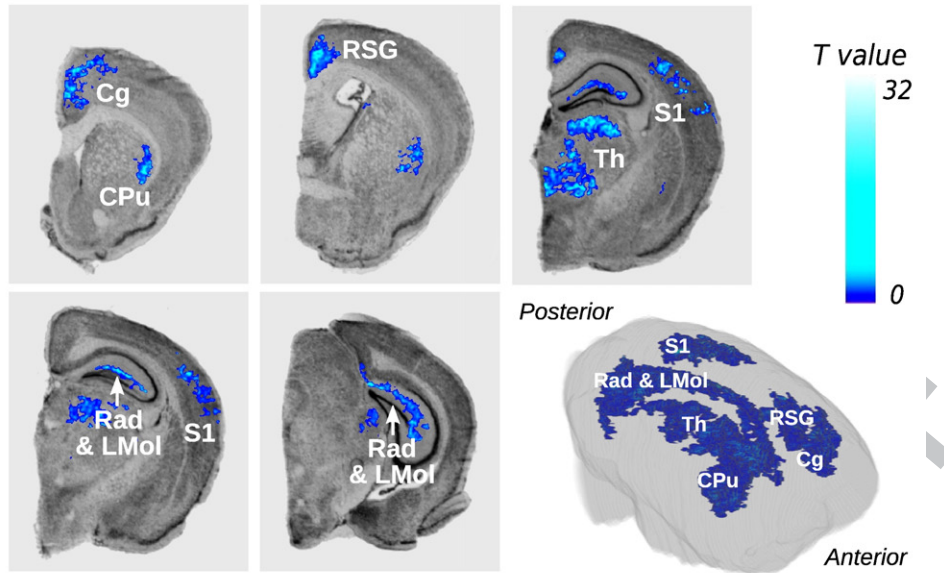
biological and medical research, demonstrating the feasibility of
 480 such an approach in mice was of prime importance. The
 481 preliminary results obtained in this pathological context highlight
 482 the likely contribution of voxel-wise analysis to assessing regional
 483 and quantitative information, to increasing knowledge about
 484 disease mechanisms and to the efficient development and exhaus-
 485 tive validation of new therapeutic approaches. This work also
 486 constitutes the first validation of such procedures for their future
 487 application to larger *post mortem* pathology data sets from
 488 transgenic animals.
 489

*Data acquisition and 3D reconstruction of blockface, histological and
 490 autoradiographic post mortem volumes* 491

492 Acquisition of blockface photographs

493 Although slightly complex (positioning on the cryostat, size, need
 494 for consistent quality and highly reproducible illumination), our
 495 blockface photograph acquisition system was well-adapted to the
 496 cryostat and provided high-quality images. Our custom-made green

Areas of lower levels of glucose uptake in APP/PS1 than in PS1 mice



Areas of higher levels of glucose uptake in APP/PS1 than in PS1 mice

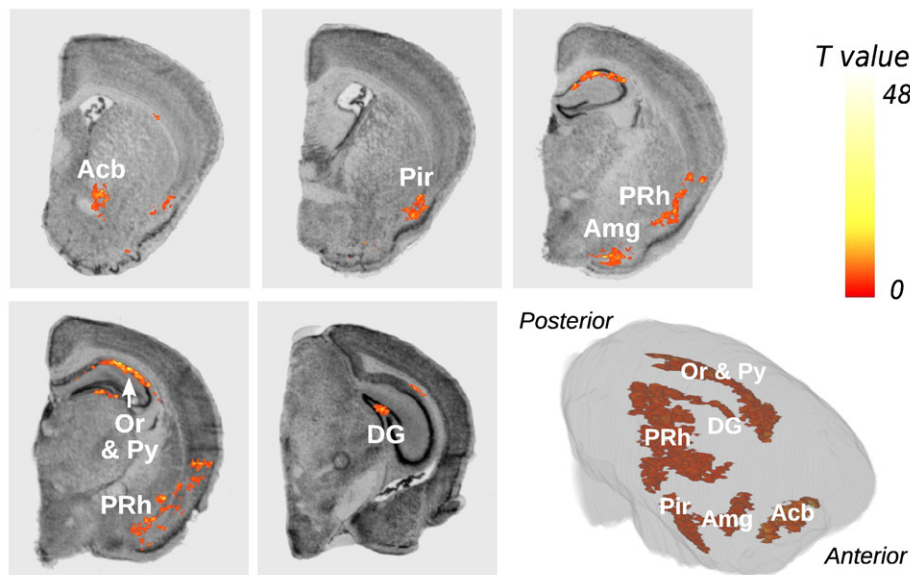


Fig. 7. Brain areas in which regional levels of glucose uptake were significantly lower (top panel, blue color scale) and higher (bottom panel, red color scale) in APP/PS1 hemispheres than in PS1 hemispheres. These areas are overlaid on several coronal stained histological sections within the spatially normalized reference mouse hemisphere. These areas are also represented as 3D volume-rendered images of the statistical t maps repositioned within the 3D volume-rendered image of the same hemisphere. Significance is indicated with t statistic color scales, corresponding to the level of significance at voxel level. Cg: cingulate cortex, CPu: striatum, RSG: retrosplenial granular cortex, Th: thalamus, S1: somatosensory cortex, Rad & LMol: radial layers and lacunosum moleculare of the CA1 and CA3 regions of the hippocampus, Acb: accumbens nucleus, Pir: piriform cortex, Amg: amygdaloid nucleus, PRh: perirhinal cortex, Or & Py: oriens and pyramidal cell layers of the CA1 and CA3 regions of the hippocampus, DG: dentate gyrus. (For interpretation of the references to color in this figure legend, the reader is referred to the web version of this article.)

497 embedding matrix gave a high level of contrast between brain tissues
 498 and background, making it possible to automate segmentation of the
 499 brain in the blockface photographs. 3D consistent blockface volumes
 500 were obtained by directly stacking the photographs, as this acquisition
 501 system guaranteed the direct alignment of all the images within
 502 the brain. The comprehensive procedure for processing blockface
 503 photographs has been integrated into BrainVISA and gathered in
 504 dedicated plugged-in modules. These latter are not yet available with
 505 BrainRAT package but might be part of its next release.

506 Nevertheless, the blockface photographs remained an intermedi-
 507 ate modality used mainly for methodology purposes since brain

tissues were unstained and blockface photographs could be acquired 508
 only remotely, with a digital camera in reflection mode. The 509
 resolution and contrast between specific brain tissues were therefore 510
 limited compared to stained histological sections. Previous works in 511
 nonhuman primates overcame some of these limitations by using a 512
 special dye injected *in vivo*. This dye enhanced the contrast on 513
 blockface photographs of *post mortem* brains (Annese et al., 2006). 514
 However, the use of such a dye would be incompatible with further 515
 quantitative [^{14}C]-2-DG autoradiography. Indeed, it requires prior 516
 fixation of the brain tissue by perfusion with 4% paraformaldehyde 517
 solution and cryopreservation by successive immersion in graded 518
 519

Table 1
Comparison of APP/PS1 and PS1 hemispheres, using the photographic template ($P < 0.01$ uncorrected for multiple comparisons; extent threshold = 1500).

Cluster level	Voxel level			Brain region			
	Pcorr	Ke	Punc	Pcorr	Punc	T	Ze
Areas of lower levels of glucose uptake in APP/PS1 than in PS1 mice							
0.000	42,892	0.000	0.103	0.000	48.25	5.39	Hippocampus (Rad and LMol of CA1 and CA3)
0.000	55,678	0.000	0.103	0.000	35.94	5.11	Thalamus
0.000	12,495	0.000	0.103	0.000	31.35	4.98	Somatosensory cortex
0.000	4760	0.000	0.103	0.000	26.89	4.84	Striatum
0.000	22,688	0.000	0.103	0.000	26.63	4.83	Cingulate cortex
0.000	3715	0.000	0.126	0.000	16.78	4.35	Striatum
0.000	2005	0.000	0.137	0.000	14.2	4.16	Striatum
0.000	2052	0.000	0.152	0.000	12.62	4.03	Retrosplenial cortex
Areas of higher levels of glucose uptake in APP/PS1 than in PS1 mice							
0.000	13,127	0.000	0.438	0.000	32.64	5.02	Hippocampus (Or and Py of CA1 and CA3)
0.000	17,676	0.000	0.528	0.000	22.67	4.66	Piriform cortex
0.000	2028	0.000	0.528	0.000	19.58	4.51	Dentate gyrus
0.000	9109	0.000	0.528	0.000	18.79	4.47	Dorsal endopiriform nucleus
0.000	5153	0.000	0.528	0.000	18.45	4.45	Amygdaloid nucleus
0.000	1983	0.000	0.528	0.000	17.91	4.42	Perirhinal cortex
0.000	4135	0.000	0.528	0.000	15.24	4.24	Accumbens nucleus

solutions of sucrose, which would wash out the 2DG trapped in the brain.

Use of the blockface volume as a 3D geometric reference

We observed that the use of individual photographs from the blockface volume as a reference for the reconstruction of histological volume was more reliable than our previously proposed method (Dubois et al., 2007). This latter, based on the block-matching rigid pairwise registration algorithm (Ourselin et al., 2001), has been intensively validated and is acknowledged to be the most comprehensive registration algorithm, in the absence of a 3D geometric reference (Malandain et al., 2004; Pitiot et al., 2006; Dauguet et al., 2007). However, it has also been criticized because if an error occurs in the registration of a section with the previous section, this error will be propagated through the entire volume (Nikou et al., 2003). If the number of sections to be registered is large, an overall offset of the volume, due to error accumulation, may occur. Obviously, this issue is more pronounced when distant sections are involved in the

Table 2
Comparison of APP/PS1 and PS1 hemispheres, using the autoradiographic template ($P < 0.01$ uncorrected for multiple comparisons; extent threshold = 1500).

Cluster level	Voxel level			Brain region			
	Pcorr	Ke	Punc	Pcorr	Punc	T	Ze
Areas of lower levels of glucose uptake in APP/PS1 than in PS1 mice							
0.000	58,218	0.000	0.128	0.000	35.71	5.11	Hippocampus (Rad and LMol of CA1 and CA3)
0.000	61,087	0.000	0.128	0.000	32.3	5.01	Thalamus
0.000	19,992	0.000	0.128	0.000	30.37	4.95	Somatosensory cortex
0.000	3161	0.000	0.128	0.000	27.08	4.84	Striatum
0.000	31,204	0.000	0.128	0.000	24.84	4.76	Cingulate and retrosplenial cortices
0.000	12,407	0.000	0.128	0.000	22.27	4.65	Striatum
Areas of higher levels of glucose uptake in APP/PS1 than in PS1 mice							
0.000	18,387	0.000	0.006	0.000	96.79	5.98	Hippocampus (Or and Py of CA1 and CA3)
0.000	9110	0.000	0.166	0.000	32.48	5.02	Dorsal endopiriform nucleus
0.000	32,702	0.000	0.166	0.000	31.72	5.00	Piriform cortex
0.000	4062	0.000	0.169	0.000	26.21	4.81	Amygdaloid nucleus
0.000	3075	0.000	0.319	0.000	10.37	3.80	Dentate gyrus
0.000	1860	0.000	0.328	0.000	9.85	3.74	Perirhinal cortex

Table 3
Regional 2-DG uptake values, mean ± standard deviation (nCi/g), percentage difference, and associated P values between APP/PS1 and PS1 mice.

Region	APP/PS1	PS1	% difference	P value
Areas of lower levels of glucose uptake in APP/PS1 than in PS1 mice				
Cingulate cortex	245 ± 12.0	345.1 ± 17.0	-35.6	<10 ⁻³
Retrosplenial cortex	275.4 ± 2.9	347.2 ± 12.9	-26.1	0.004
Thalamus	259.6 ± 3.6	334.5 ± 11.4	-28.8	0.002
Somatosensory cortex	267.8 ± 3.2	330.2 ± 11.0	-23.3	0.004
Hippocampus (Rad and LMol of CA1 and CA3)	241.6 ± 5.4	301.1 ± 7.0	-24.6	<10 ⁻³
Striatum	242.9 ± 6.9	297.2 ± 8.8	-22.4	0.001
Areas of higher levels of glucose uptake in APP/PS1 than in PS1 mice				
Perirhinal cortex	271.5 ± 4.1	227.7 ± 4.2	19.3	<10 ⁻³
Piriform cortex	303.7 ± 5.8	250.0 ± 7.3	21.5	<10 ⁻³
Dorsal endopiriform nucleus	20.8 ± 12.5	239.9 ± 5.1	33.7	<10 ⁻³
Accumbens nucleus	297.9 ± 4.8	247.4 ± 1.7	20.4	<10 ⁻³
Amygdaloid nucleus	311.6 ± 11.3	253.5 ± 3.1	22.9	0.001
Dentate gyrus	238.1 ± 6.4	190.1 ± 6.4	25.2	<10 ⁻³
Hippocampus (Or and	236.7 ± 5.0	188.2 ± 6.0	25.8	<10 ⁻³

registration. Thus, a modification of the global shape of the 3D reconstructed volume may be observed. Moreover, in the absence of a 3D geometric reference, a rigid pairwise registration of 2D sections does not provide a volume with the real geometry of the object under study (i.e., the brain after extraction from the skull but before sectioning and staining). Indeed, another major difficulty in the reconstruction of a 3D volume from 2D sections comes from the so-called “banana problem”: a curved 3D object cannot be reconstructed from cross-sections in the absence of additional information (Streicher et al., 1997; Malandain et al., 2004). By providing additional information about the real geometry of the object under study, the co-alignment of the 2D histological sections with the corresponding blockface photographs made it possible to preserve the 3D curvature of the *post mortem* brain, thereby overcoming the “banana problem”. We also showed that a propagation-based approach was locally more reliable than the use of individual photographs from the blockface volume as a reference for the reconstruction of histological volume. Indeed, the contrast between specific brain tissues and resolution of Nissl-stained histological sections were higher as compared to blockface photographs. Nissl-stained sections provide greater anatomical detail than blockface photographs, hence allowing their locally more accurate matching on consecutive sections. However, the differences were really subtle and mainly located in strongly contrasting structures, which did not justify ignoring the value of blockface photographs for preserving the 3D curvature of the *post mortem* brain.

Anatomy as a reference for the 3D reconstruction of autoradiographic data sets

The use of the histological volume as a reference for the reconstruction of the autoradiographic volume provided the finest section-by-section superimpositions of histological and autoradiographic volumes, to the scale of Aβ plaques (~100 μm in diameter), as shown in Fig. 6, thereby giving the best inter-volume consistency. Hence, the global strategy we proposed for the 3D reconstruction of histological and autoradiographic volumes optimized both intra- and inter-volume consistency as well as the use of the three imaging techniques available in this study.

The block-matching registration technique is based on both the section edges and the whole image, so the result of the 3D reconstruction depends on the type of data processed, corresponding to the information available from the sections. The independent co-registration of histological and autoradiographic sections with the corresponding blockface photographs, despite relating to the same physical sections, did not give identical results or perfect section-by-

580 section anatomical and functional superimposition. By contrast, the
581 use of the reconstructed histological volume (resulting from the
582 registration of histological sections with the corresponding photo-
583 graphs) as a reference for reconstruction of the functional volume
584 ensured an identical 3D geometry for the final two volumes.

585 Thus, the best overall method for the 3D reconstruction of both
586 histological and autoradiographic volumes combined the intrinsic
587 spatial consistency of the blockface volume with the high-quality
588 contrast and structural accuracy of histological information. The
589 blockface volume and the 3D-reconstructed histological and autora-
590 diographic volumes not only had similar geometries, but their
591 anatomical and functional co-registration was optimal.

592 Spatial normalization

593 We previously demonstrated (Dubois et al., 2008b) that an
594 autoradiographic template was more appropriate for spatial normal-
595 ization (pre-requisite to voxel-wise statistical analysis) than a
596 histological template. Here, we compared an autoradiographic to a
597 photographic template-based spatial normalization technique.

598 The intensity-based approach used for the non-linear spatial
599 normalization procedure minimizes the sum of squared differences
600 between the images to be normalized and the template. The best
601 procedure must provide the smallest standard deviation values. Free
602 from potential between-group differences between PS1 and APP/PS1
603 mice, standard deviation images showed similar values and thus
604 demonstrated that the intensity differences between the images and
605 the template were equivalently reduced by the two different spatial
606 normalization techniques. Moreover, the photographic and autora-
607 diographic template-based methods also gave similar results in terms
608 of its influence on the detection of functional differences between
609 animals. However, we preferred the photographic template-based
610 method over the autoradiographic method for two reasons. First,
611 blockface imaging provides a consistent 3D geometric reference free
612 from possible deformation artefacts associated with the sectioning
613 process (displacements, torn or missing parts, folds). Non-linear
614 transformations, such as those used in SPM5, are generally more
615 sensitive to these artefacts, because they include larger numbers of
616 degrees of freedom than linear transformations. Consequently,
617 estimation of the non-linear transformations between photographic
618 volumes and the corresponding template image should give more
619 accurate results than estimation based on autoradiographic volumes.
620 Second, unlike autoradiography, blockface photographs are unbiased
621 in terms of the functional changes studied and the photographic
622 template-based normalization method therefore prevents possible
623 misregistrations due to differences in intensity between animals
624 resulting from their physiological and/or pathological status or the
625 experimental paradigm used.

626 Statistical analysis and biological assessments

627 Few studies have evaluated changes in cerebral glucose uptake in
628 transgenic mouse models of AD. The reported studies to date have
629 been realized by a classical ROI-based analysis of autoradiographic
630 data. The authors observed progressive decreases in glucose uptake
631 within some cerebral structures (Hsiao et al., 1996; Dodart et al.,
632 1999; Niwa et al., 2002; Sadowski et al., 2004; Valla et al., 2006),
633 including the posterior cingulate cortex in particular (Reiman et al.,
634 2000; Valla et al., 2008). Some of them have also reported an increase
635 in glucose uptake particularly within the cortex, the hippocampus and
636 the striatum. However, evidence for statistically significant variations
637 in glucose uptake was often provided after further segmentation of
638 “meta-structures” like the hippocampal formation.

639 The present study is therefore the first to report changes in
640 cerebral glucose uptake in transgenic mouse models of AD obtained
641 by using a fully automated whole-brain analysis without any

642 anatomical *a priori*. Thus, we detected significantly lower levels of
643 cerebral glucose uptake in APP/PS1 than PS1 mice, within the
644 hippocampus (lacunosum moleculare and radial layers of the CA1
645 region), the cortex, the striatum and the thalamus. We also identified
646 regions with significantly higher levels of cerebral glucose uptake.
647 These regions included cortical areas, the amygdala, the dorsal
648 endopiriform and accumbens nuclei, the dentate gyrus and the dorsal
649 part of the hippocampus (the oriens and pyramidal cell layers of the
650 CA1 and CA3 regions). The APP/PS1 mice we studied are known to
651 show only slight neuronal loss, as demonstrated by comparisons with
652 PS1 mice (Blanchard et al., 2003). However, these mice have been
653 reported to display changes in behavior (Cudennec et al., 2008). Our
654 results highlight a complex pattern of decreases and increases in
655 glucose uptake in various brain areas, which might account for some
656 of the behavioral changes in these animals. These findings are
657 consistent with the results of other studies in the APP/PS1 transgenic
658 mouse model of AD (Sadowski et al., 2004). The precise cause of these
659 changes in glucose uptake however remains to be determined. A
660 causal relationship between the impairment of glucose utilization in
661 APP/PS1 mice and A β accumulation may be suggested. Future
662 investigations are therefore required. They could benefit from the
663 use of neuropathology-free PS1 littermates (they do not display
664 amyloid deposits) as controls so as to specifically assess the APP
665 related effects of amyloid deposition on brain metabolism.

666 As mentioned above, individual regions of lower and higher levels
667 of glucose uptake than for PS1 mice were concomitantly detected
668 within the hippocampus of APP/PS1 mice (Fig. 8). To the best of our
669 knowledge, this is the first report of such differences. This original
670 result may be accounted for by conceptual differences between
671 previous studies, based on conventional ROI analysis, and this study,
672 based on voxel-wise analysis. Indeed, voxel-wise analysis automati-
673 cally provides statistical between-group differences, whereas ROI-
674 based analysis is dependent on the subjective placement of ROIs. For
675 brain structures with irregular borders or a mosaic organization of
676 afferent and efferent projections, it remains difficult to define ROIs
677 accurately. This is precisely the case for the hippocampus, the
678 complex shape of which makes it difficult to place the corresponding

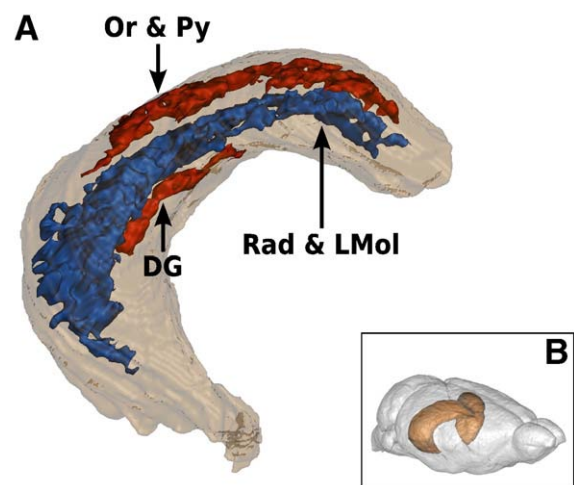


Fig. 8. (A) Clusters of significantly lower (blue) and higher (red) levels of glucose uptake in APP/PS1 than in PS1 mice, obtained within the hippocampus, are represented as 3D surface renderings. They are also repositioned within a 3D volume-rendering of the hippocampal region, manually delineated on the histological volume of the reference hemibrain, previously spatially normalized using the deformation parameters derived from the corresponding blockface volume. The orientation of the hippocampus is indicated by (B). Rad & LMol: radial layers and lacunosum moleculare of CA1 and CA3 regions of the hippocampus and DG: dentate gyrus. (For interpretation of the references to color in this figure legend, the reader is referred to the web version of this article.)

ROI exactly. We calculated that the regions displaying lower and higher levels of glucose uptake within the hippocampus encompassed only 11% and 3% of the total volume of the hippocampus, respectively. Given these low percentages, some of the corresponding information might be unexploited, or even missed, in a classic ROI-based approach.

Nevertheless, there are some limitations associated with the present study. First, our preliminary results are obviously severely limited by the small sample size ($n = 7$). Caution must be applied, as the findings might not be extended to any population of APP/PS1 transgenic mice. However, they tend to show that voxel-wise statistical analysis may constitute a reliable alternative to classical ROI-based approaches, allowing biologists both to improve their understanding of the pathophysiology of AD and the investigation of the efficacy of new treatments. Second, methods combining data from different subjects into a common spatial referential may encounter issues related to final spatial resolution or image deformation. We performed analyses with different smoothing extents (isotropic and anisotropic Gaussian kernel widths) and found no major differences in the location of detected clusters and their spatial extents (data not shown). As mentioned by Nguyen et al. (2004), the observed cluster size depends on the intrinsic resolution of the data and the inter-section spacing. Thus, interpretation of clusters is based on neuroanatomic correlation, as adjacent regions may fuse into a single cluster. As regards image deformation, the underlying assumption in employing the anatomical standardization of an individual subject image is that the intersubject anatomical variability should be within the range of the values expected by the spatial normalization algorithm. In the present study, this assumption may be unrealistic since different mouse strains are more variable than rats in brain anatomy and APP/PS1 transgenic mice exhibit anatomical abnormalities. Indeed, as previously described (Delatour et al., 2006), aged (24 months) APP/PS1 mice showed a moderate global brain atrophy in posterior brain regions as compared to age-matched PS1 animals. The impact of image deformation was however reduced by the use of a study-specific template, which was generated by averaging the individual images spatially normalized onto an initial target hemisphere. Thus, we minimized registration errors between the images and the template due to the possible singularity in the selected target hemisphere. Third, we reported significant results that only reached $P < 0.01$ uncorrected for multiple comparisons. As we pointed out (Dubois et al., 2008b), to obtain results that meet the community standards for statistical significance ($P < 0.05$ corrected for multiple comparisons), prior assumptions must be made to reduce the number of voxels to be compared. We are therefore currently developing a strategy for automatically defining anatomically relevant volumes of interest so that only specific subdivisions of the brain are analyzed for significant regions. Our strategy is based on the registration of an MRI-based 3D digital atlas of the mouse brain with the 3D-reconstructed *post mortem* data (personal communication: (Lebenberg et al., 2009)). Lastly, since no young animals were studied, additional studies are needed to determine which of the reported changes in glucose uptake reflect progressive pathology, and how they are related to the time course of amyloid pathology.

Conclusion

We showed the feasibility of applying computerized procedures for the acquisition, 3D reconstruction, spatial normalization and voxel-wise statistical analysis to autoradiographic data sets mapping brain metabolic activity in a mouse model of AD. To the best of our knowledge, this work is the first validation study of such an approach in a mouse model of human neurodegenerative disease. Using only seven mice, we obtained preliminary results that appear to be meaningful, consistent, and more comprehensive than findings from previously published studies based on conventional ROI-based methods. The establishment of statistical significance at the voxel

level, rather than with a user-defined ROI, made it possible to detect subtle differences in geometrically complex regions, such as the hippocampus, more reliably. We also provided the first demonstration of the value of blockface photographs for the 3D reconstruction and spatial normalization of *post mortem* mouse brain volumes. The use of individual photographs from the blockface volume as a reference for the reconstruction of histological volume ensures greater intravolume consistency and robustness than our previously published approach (Dubois et al., 2007). Blockface photographs are also free from possible deformation artefacts associated with the sectioning process and unbiased in terms of the functional changes studied, both facilitating the spatial normalization.

By allowing an operator-independent analysis and guaranteeing objective results, this approach might also constitute a standardized method for the objective comparison of changes in cerebral glucose utilization across ages and between lines of transgenic mice. This method could be more widely used in animal models of various human neurodegenerative diseases to establish relationships between histopathological features and regional brain function, to help clarify disease mechanisms, and to screen candidate treatments, guiding their selection for testing in expensive, time-consuming preclinical trials.

Acknowledgment

We would like to thank the Sanofi-Aventis Neurodegenerative Disease Group for generously providing the transgenic animals involved in this study.

References

- Annese, J., Sforza, D.M., Dubach, M., Bowden, D., Toga, A.W., 2006. Postmortem high-resolution 3-dimensional imaging of the primate brain: blockface imaging of perfusion stained tissue. *Neuroimage* 30 (1), 61–69.
- Ashburner, J., Friston, K.J., 1999. Nonlinear spatial normalization using basis functions. *Hum. Brain Mapp.* 7 (4), 254–266.
- Blanchard, V., Moussaoui, S., Czech, C., Touchet, N., Bonici, B., Planche, M., Canton, T., Jedidi, I., Gohin, M., Wirths, O., Bayer, T.A., Langui, D., Duyckaerts, C., Tremp, G., Pradier, L., 2003. Time sequence of maturation of dystrophic neurites associated with Abeta deposits in APP/PS1 transgenic mice. *Exp. Neurol.* 184 (1), 247–263.
- Brett, M., Valabregue, R., Poline, J.-B., 2003. Region of interest analysis using an SPM toolbox (abstract). *Neuroimage* 16 ((Suppl.)) (CD-ROM).
- Cudennec, C.L., Faure, A., Ly, M., Delatour, B., 2008. One-year longitudinal evaluation of sensorimotor functions in APP751SL transgenic mice. *Genes Brain Behav.* 7 (Suppl 1), 83–91.
- Dauguet, J., Delzescaux, T., Condé, F., Mangin, J.-F., Ayache, N., Hantraye, P., Frouin, V., 2007. Three-dimensional reconstruction of stained histological slices and 3D nonlinear registration with in-vivo MRI for whole baboon brain. *J. Neurosci. Methods* 164 (1), 191–204.
- Delatour, B., Guégan, M., Volk, A., Dhenain, M., 2006. In vivo MRI and histological evaluation of brain atrophy in APP/PS1 transgenic mice. *Neurobiol. Aging* 27 (6), 835–847.
- Dhenain, M., El Tannir El Tayara, N., Wu, T.-D., Guégan, M., Volk, A., Quintana, C., Delatour, B., 2009. Characterization of in vivo MRI detectable thalamic amyloid plaques from APP/PS1 mice. *Neurobiol. Aging* 30 (1), 41–53.
- Dodart, J.C., Mathis, C., Bales, K.R., Paul, S.M., Ungerer, A., 1999. Early regional cerebral glucose hypometabolism in transgenic mice overexpressing the V717F beta-amyloid precursor protein. *Neurosci. Lett.* 277 (1), 49–52.
- Dubois, A., Dauguet, J., Hérard, A.-S., Besret, L., Duchesnay, E., Frouin, V., Hantraye, P., Bonvento, G., Delzescaux, T., 2007. Automated three-dimensional analysis of histological and autoradiographic rat brain sections: application to an activation study. *J. Cereb. Blood Flow. Metab.* 27 (10), 1742–1755.
- Dubois, A., Dauguet, J., Souedet, N., Hérard, A.-S., Rivière, D., Cointepas, Y., Bonvento, G., Hantraye, P., Frouin, V., Delzescaux, T., 2008a. BrainRAT: Brain Reconstruction and Analysis Toolbox. A freely available toolbox for the 3D reconstruction of anatomofunctional brain sections in rodents. 38th Annual Meeting of the Society for Neuroscience. Washington, USA.
- Dubois, A., Hérard, A.-S., Flandin, G., Duchesnay, E., Besret, L., Frouin, V., Hantraye, P., Bonvento, G., Delzescaux, T., 2008b. Quantitative validation of voxel-wise statistical analyses of autoradiographic rat brain volumes: application to unilateral visual stimulation. *Neuroimage* 40 (2), 482–494.
- Duff, K., Eckman, C., Zehr, C., Yu, X., Prada, C.M., Perez-tur, J., Hutton, M., Buee, L., Harigaya, Y., Yager, D., Morgan, D., Gordon, M.N., Holcomb, L., Refolo, L., Zenk, B., Hardy, J., Younkin, S., 1996. Increased amyloid-beta42(43) in brains of mice expressing mutant presenilin 1. *Nature* 383 (6602), 710–713.
- El Tannir El Tayara, N., Delatour, B., Cudennec, C.L., Guégan, M., Volk, A., Dhenain, M., 2006. Age-related evolution of amyloid burden, iron load, and MR relaxation times

- 816 in a transgenic mouse model of Alzheimer's disease. *Neurobiol. Dis.* 22 (1),
817 199–208.
- 818 Games, D., Adams, D., Alessandrini, R., Barbour, R., Berthelette, P., Blackwell, C., Carr, T.,
819 Clemens, J., Donaldson, T., Gillespie, F., 1995. Alzheimer-type neuropathology in
820 transgenic mice overexpressing V717F beta-amyloid precursor protein. *Nature* 373
821 (6514), 523–527.
- 822 Goedert, M., Spillantini, M.G., 2006. A century of Alzheimer's disease. *Science* 314
823 (5800), 777–781.
- 824 Holcomb, L., Gordon, M.N., McGowan, E., Yu, X., Benkovic, S., Jantzen, P., Wright, K.,
825 Saad, I., Mueller, R., Morgan, D., Sanders, S., Zehr, C., O'Campo, K., Hardy, J., Prada, C.
826 M., Eckman, C., Younkin, S., Hsiao, K., Duff, K., 1998. Accelerated Alzheimer-type
827 phenotype in transgenic mice carrying both mutant amyloid precursor protein and
828 presenilin 1 transgenes. *Nat. Med.* 4 (1), 97–100.
- 829 Holschneider, D.P., Maarek, J.-M.I., 2008. Brain maps on the go: functional imaging
830 during motor challenge in animals. *Methods* 45 (4), 255–261.
- 831 Holschneider, D.P., Yang, J., Sadler, T.R., Nguyen, P.T., Givrad, T.K., Maarek, J.-M.I., 2006.
832 Mapping cerebral blood flow changes during auditory-cued conditioned fear in the
833 nonthreatened, nonrestrained rat. *Neuroimage* 29 (4), 1344–1358.
- 834 Hsiao, K., Chapman, P., Nilsen, S., Eckman, C., Harigaya, Y., Younkin, S., Yang, F., Cole, G.,
835 1996. Correlative memory deficits, Abeta elevation, and amyloid plaques in
836 transgenic mice. *Science* 274 (5284), 99–102.
- 837 Klunk, W.E., Engler, H., Nordberg, A., Wang, Y., Blomqvist, G., Holt, D.P., Bergström, M.,
838 Savitcheva, I., Huang, G.-F., Estrada, S., Ausén, B., Debnath, M.L., Barletta, J., Price, J.
839 C., Sandell, J., Lopresti, B.J., Wall, A., Koivisto, P., Antoni, G., Mathis, C.A., Långström,
840 B., 2004. Imaging brain amyloid in Alzheimer's disease with Pittsburgh Compound-
841 B. *Ann. Neurol.* 55 (3), 306–319.
- 842 Lebenberg, J., Hérad, A.-S., Dubois, A., Dhenain, M., Hantraye, P., Frouin, V., Delzescaux,
843 T., 2009. Segmentation of anatomo-functional 3D post mortem data using a MRI-
844 based 3D digital atlas: transgenic mouse brains study. The Sixth IEEE International
845 Symposium on Biomedical Imaging. Boston, USA.
- 846 Lee, J., Ahn, S.-H., Lee, D., Oh, S., Kim, C., Jeong, J., Park, K., Chung, J.-K., Lee, M., 2005.
847 Voxel-based statistical analysis of cerebral glucose metabolism in the rat cortical
848 deafness model by 3D reconstruction of brain from autoradiographic images. *Eur. J.*
849 *Nucl. Med. Mol. Imaging* 32 (6), 696–701.
- 850 Malandain, G., Bardinet, E., Nelissen, K., Vanduffel, W., 2004. Fusion of autoradiographs
851 with an MR volume using 2-D and 3-D linear transformations. *NeuroImage* 23 (1),
852 111–127.
- 853 Minoshima, S., Giordani, B., Berent, S., Frey, K.A., Foster, N.L., Kuhl, D.E., 1997. Metabolic
854 reduction in the posterior cingulate cortex in very early Alzheimer's disease. *Ann.*
855 *Neurol.* 42 (1), 85–94.
- 856 Nguyen, P., Holschneider, D., Maarek, J., Yang, J., Mandelkern, M., 2004. Statistical
857 parametric mapping applied to an autoradiographic study of cerebral activation
858 during treadmill walking in rats. *NeuroImage* 23 (1), 252–259.
- Nikou, C., Heitz, F., Nehlig, A., Namer, I., Armspach, J., 2003. A robust statistics-based
global energy function for the alignment of serially acquired autoradiographic
sections. *J. Neurosci. Methods* 124 (1), 93–102.
- Niwa, K., Kazama, K., Younkin, S.G., Carlson, G.A., Iadecola, C., 2002. Alterations in
cerebral blood flow and glucose utilization in mice overexpressing the amyloid
precursor protein. *Neurobiol. Dis.* 9 (1), 61–68.
- Ourselin, S., Roche, A., Subsol, G., Pennec, X., Ayache, N., 2001. Reconstructing a 3D
structure from serial histological sections. *Image Vis. Comput.* 19 (1–2), 25–31.
- Paxinos, G., Franklin, K., 2001. *The Mouse Brain in Stereotaxic Coordinates*. Academic
Press, San Diego, CL.
- Pitiot, A., Bardinet, E., Thompson, P.M., Malandain, G., 2006. Piecewise affine
registration of biological images for volume reconstruction. *Med. Image Anal.* 10
(3), 465–483.
- Reiman, E.M., Caselli, R.J., Yun, L.S., Chen, K., Bandy, D., Minoshima, S., Thibodeau, S.N.,
Osborne, D., 1996. Preclinical evidence of Alzheimer's disease in persons homozygous
for the epsilon 4 allele for apolipoprotein E. *N. Engl. J. Med.* 334 (12), 752–758.
- Reiman, E.M., Uecker, A., Gonzalez-Lima, F., Minear, D., Chen, K., Callaway, N.L., Berndt, J.
D., Games, D., 2000. Tracking Alzheimer's disease in transgenic mice using
fluorodeoxyglucose autoradiography. *NeuroReport* 11 (5), 987–991.
- Sadowski, M., Pankiewicz, J., Scholtzova, H., Ji, Y., Quartermain, D., Jensen, C.H., Duff, K.,
Nixon, R.A., Gruen, R.J., Wisniewski, T., 2004. Amyloid-beta deposition is associated
with decreased hippocampal glucose metabolism and spatial memory impairment
in APP/PS1 mice. *J. Neuropathol. Exp. Neurol.* 63 (5), 418–428.
- Shoghi-Jadid, K., Small, G.W., Agdeppa, E.D., Kepe, V., Ercoli, L.M., Siddarth, P., Read, S.,
Satyamurthy, N., Petric, A., Huang, S.-C., Barrio, J.R., 2002. Localization of
neurofibrillary tangles and beta-amyloid plaques in the brains of living patients
with Alzheimer disease. *Am. J. Geriatr. Psychiatry* 10 (1), 24–35.
- Small, G.W., Kepe, V., Ercoli, L.M., Siddarth, P., Bookheimer, S.Y., Miller, K.J., Lavretsky,
H., Burggren, A.C., Cole, G.M., Vinters, H.V., Thompson, P.M., Huang, S.-C.,
Satyamurthy, N., Phelps, M.E., Barrio, J.R., 2006. PET of brain amyloid and tau in
mild cognitive impairment. *N. Engl. J. Med.* 355 (25), 2652–2663.
- Streicher, J., Weninger, W.J., Müller, G.B., 1997. External marker-based automatic
congruencing: a new method of 3D reconstruction from serial sections. *Anat. Rec.*
248 (4), 583–602.
- Valla, J., Schneider, L., Reiman, E.M., 2006. Age- and transgene-related changes in
regional cerebral metabolism in PSAPP mice. *Brain Res.* 1116 (1), 194–200.
- Valla, J., Gonzalez-Lima, F., Reiman, E.M., 2008. FDG autoradiography reveals
developmental and pathological effects of mutant amyloid in PDAPP transgenic
mice. *Int. J. Dev. Neurosci.* 26 (3–4), 253–258.
- Wirhith, O., Multhaup, G., Czech, C., Blanchard, V., Moussaoui, S., Tremp, G., Pradier, L.,
Beyreuther, K., Bayer, T.A., 2001. Intraneuronal Abeta accumulation precedes
plaque formation in beta-amyloid precursor protein and presenilin-1 double-
transgenic mice. *Neurosci. Lett.* 306 (1–2), 116–120.